



HAL
open science

Measurement of fracture energy during single-particle fracture

R. Peter King, Florent Bourgeois

► **To cite this version:**

R. Peter King, Florent Bourgeois. Measurement of fracture energy during single-particle fracture. Minerals Engineering, 1993, 4, pp.353-357. 10.1016/0892-6875(93)90015-F . hal-02135531

HAL Id: hal-02135531

<https://hal.science/hal-02135531>

Submitted on 21 May 2019

HAL is a multi-disciplinary open access archive for the deposit and dissemination of scientific research documents, whether they are published or not. The documents may come from teaching and research institutions in France or abroad, or from public or private research centers.

L'archive ouverte pluridisciplinaire **HAL**, est destinée au dépôt et à la diffusion de documents scientifiques de niveau recherche, publiés ou non, émanant des établissements d'enseignement et de recherche français ou étrangers, des laboratoires publics ou privés.



OATAO is an open access repository that collects the work of Toulouse researchers and makes it freely available over the web where possible

This is an author's version published in: <http://oatao.univ-toulouse.fr/3541>

Official URL : [https://doi.org/10.1016/0892-6875\(93\)90015-F](https://doi.org/10.1016/0892-6875(93)90015-F)

To cite this version :

King, R. Peter and Bourgeois, Florent  *Measurement of fracture energy during single-particle fracture.* (1993) *Minerals Engineering*, (4). 353-357. ISSN 0892-6875

Any correspondence concerning this service should be sent to the repository administrator: tech-oatao@listes-diff.inp-toulouse.fr

MEASUREMENT OF FRACTURE ENERGY DURING SINGLE-PARTICLE FRACTURE

R.P. KING and F. BOURGEOIS

Comminution Center, University of Utah, 306 WBB,
Salt Lake City, UT 84112, USA

(Received 12 October 1992; accepted 30 October 1992)

ABSTRACT

The population balance model provides a very good description of the comminution of brittle particulate material. The breakage function plays a central role in the population balance method and its variation with impact energy is now considered to be important when scaling up data for operating ball mills. The rate of breakage has been known for many years to be impact-energy dependent. This paper describes the operation and calibration of a precise apparatus for the measurement of the distribution of fracture energies among particles and the relationship between the breakage function and the impact energy. The distribution of fracture energies was found to be log normal and varies consistently with particle size. The distribution of fracture energy for several different materials was determined. The one-to-one correspondence between the probability of breakage and the distribution of fracture energies is demonstrated.

Keywords

Fracture, energy, impact

INTRODUCTION

The population balance model provides a very good description of the comminution of brittle particulate material. The breakage function plays a central role in the population balance method. The breakage function describes the distribution of daughter fragments after a fracture event and a correct prediction of the breakage function is essential to the successful use of the population balance method for the description of industrial comminution machines. The breakage function results from the complex fragmentation processes that occur when a brittle particle is stressed beyond its strength and fragmentation results. The material properties of the particle as well as the nature of the stress application process influence the breakage function. Very little is known about the precise relationship among these complex factors and this paper describes a careful experimental program that was undertaken to measure the breakage function and the distribution of fracture energies during well-controlled single-particle impact-fracture tests.

A device, which has been called the ultrafast load cell (UFLC), was developed at the Utah Comminution Center for the study of the impact fracture of single particles and beds of particles of brittle material. This device is capable of recording the force-time history experienced by the particles during the impact. The time resolution of the device is 1 μ s and, because the impact events to be studied range in total duration from 50 to several hundred microseconds, specific details of the fracture process may easily be observed. The precise measurement of the force experienced by the particles during impact permits the measurement of some fundamental properties of the particulate material including the energy absorbed by the particle prior to initial fracture and the relationship between this energy and the breakage function.

CALIBRATION OF THE ULTRA-FAST LOAD CELL

The UFLC is capable of very precise measurements and a particular advantage of the device is that it can be calibrated absolutely using a well-defined straight-forward procedure. The calibration procedure is reported here in some detail.

The UFLC is constructed as a Hopkinson bar that is oriented vertically. The general layout of the UFLC is shown in Figure 1.

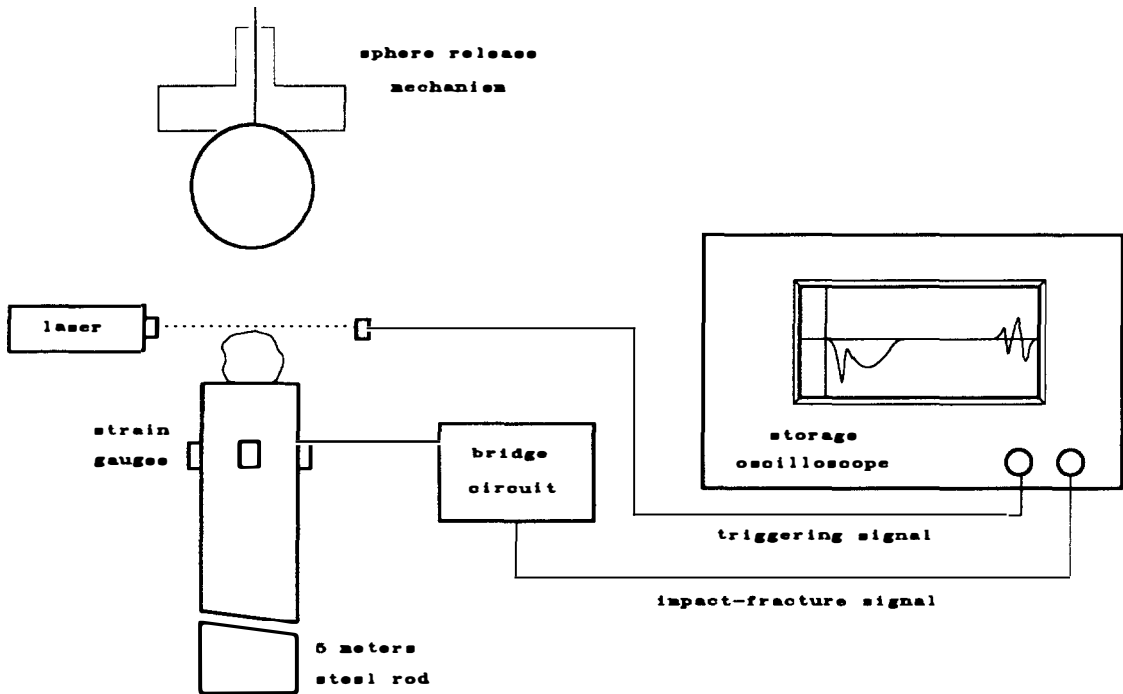


Fig.1 Schematic outline of the ultra-fast load cell. The sphere release mechanism can be adjusted vertically to vary the drop height of the impacting sphere.

The calibration impact is induced at the top face of the bar by dropping a steel ball onto the face. The impact on the top face causes a compressive strain wave to travel downwards through the rod. In spite of the very small area of contact during impact, the compressive wave spreads uniformly across the rod cross-section within the first few cm of travel. The resulting planar compressive strain wave is recorded as it passes an array of strain gauges that is fixed to the rod 17.7 cm from the top.

The calibration procedure consists in recording the strain wave that results from the impact of a steel sphere of known diameter dropped from a known elevation. The dynamics of the impact under these conditions are well understood so that the response the UFLC should produce can be accurately predicted. The comparison of the measured and predicted response provides an accurate check on the calibration constant of the load cell array and also can identify if any filtering of the output exists that will lead to the loss of high-frequency information in the stress wave.

The theoretical modeling of the high-speed impact of an elastic sphere on the end of a uniform bar is completely described in Goldsmith [1]. Consider the vertical bar shown in Figure 1. A plane compressive strain wave will be propagated down the rod according to

$$\frac{\partial^2 \Delta}{\partial t^2} = \frac{E}{\rho} \frac{\partial^2 \Delta}{\partial x^2} \quad (1)$$

where $\Delta = \partial u_x / \partial x$ is the local strain [1], u_x is the local displacement in the rod, E is the elastic modulus of the rod material, and ρ its density.

Equation (1) shows that a plane compressive strain wave propagates down the rod with velocity

$$c_o = \left(\frac{E}{\rho} \right)^{1/2} \quad (2)$$

The shape of the strain pulse induced at the top of the rod can be calculated from the known dynamics of the impact between the sphere and the top of the rod. This is known as the Hertz impact problem and is comprehensively described in Goldsmith [1].

During the impact, both the rod and the sphere are compressed by amounts that vary from zero at the instant of first contact to a maximum when the ball is stationary after which the rebound commences. The compression in the rod is represented by u_1 while the sphere center moves a distance u_2 as illustrated in Figure 2. The force exerted by the sphere on the top surface of the rod is determined primarily by the relative compression of the two bodies which is given by $\alpha = u_2 - u_1$ and, for Hertzian impact, this force can be shown to be given by [1]

$$F = k(u_2 - u_1)^{3/2} \quad (3)$$

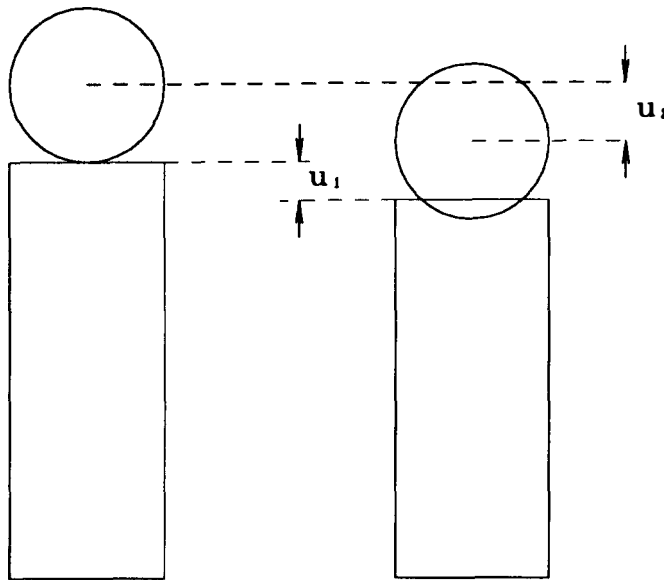


Fig.2 Diagram showing the displacements in the impacting sphere and the top of the rod during impact.

k is a function of the geometry and material properties of the sphere and the rod and in the present case is given by

$$k = \frac{4}{3} \frac{0.3180 R^{1/2}}{\delta_1 + \delta_2} \quad (4)$$

with

$$\delta_i = \frac{1 - \mu_i^2}{E_i \pi} \quad (5)$$

and R is the radius of the sphere; μ_i the Poisson ratio and E_i the Young's Modulus for each of the two materials. k can be calculated from the known properties of the rod and ball. Equations (3) - (5) constitute the so-called Hertz law of impact and they have been verified experimentally under a variety of situations and this law is regarded as providing a precise specification of the force that is experienced by the upper face of the UFLC during the ball-only impact.

The stress wave that is generated in the rod of the UFLC, due to the impacting sphere, can be calculated by a momentum balance on the impacting sphere at the top end of the rod. The displacement of the upper end of the rod is governed by the elastic properties of the rod material and the instantaneous force on the surface

$$F/A = -E\Delta \quad \text{at } x = 0 \quad (6)$$

This can be related to the rate of transmission of the strain wave by

$$\left(\frac{\partial u_x}{\partial x} \right)_t \left(\frac{\partial x}{\partial t} \right)_{u_x} \left(\frac{\partial t}{\partial u_x} \right)_x = -1 \quad (7)$$

from which

$$\Delta = \left(\frac{\partial u_x}{\partial x} \right)_t = -\frac{1}{c_o} \left(\frac{\partial u_x}{\partial t} \right)_x \quad (8)$$

where

$$c_o = \left(\frac{\partial x}{\partial t} \right)_{u_x} \quad (9)$$

is by definition the rate of transmission of the strain wave. The end condition (6) can be written using Eqs. (2) and (8)

$$F = \rho A c_o \frac{du_1}{dt} \quad (10)$$

The motion of the sphere during the impact is determined by a simple momentum balance

$$m \frac{d^2 u_2}{dt^2} = -F + mg \quad (11)$$

The variation of the relative compression is given by

$$\begin{aligned}
 \frac{d^2\alpha}{dt^2} &= \frac{d^2u_2}{dt^2} - \frac{d^2u_1}{dt^2} \\
 &= \frac{-F}{m} + g - \frac{1}{\rho A c_o} \frac{dF}{dt} \\
 &= \frac{-k\alpha^{3/2}}{m} + g - \frac{3k\alpha^{1/2}}{2\rho A c_o} \frac{d\alpha}{dt}
 \end{aligned} \tag{12}$$

This second-order differential equation is best solved numerically as two simultaneous first-order equations

$$\begin{aligned}
 \frac{d\alpha}{dt} &= y \\
 \frac{dy}{dt} &= \frac{-k\alpha^{3/2}}{m} + g - \frac{3}{2} \frac{k\alpha^{1/2}}{\rho A c_o} y
 \end{aligned} \tag{13}$$

with initial conditions

$$\begin{aligned}
 y &= V_o & \text{at } t = 0 \\
 \alpha &= 0 & \text{at } t = 0
 \end{aligned} \tag{14}$$

V_o is the known velocity of approach of the sphere immediately prior to impact.

The numerical solution of Eqs. (14) is not difficult and the force on the upper face of the UFLC rod can be recovered from the solution using Eq. (3).

$$F = k\alpha^{3/2} \tag{15}$$

Solutions for tests using several different ball drop heights are shown in Figures 6-9.

Four strain gauges were bonded to the rod as shown in Figure 3. This arrangement of the strain gauges around the circumference of the rod ensured that the measurements were compensated for any bending of the rod. The strain-gauge bridge was setup as shown in Figure 3.

The resistance of the unbonded strain gauges was 2316.5 ohms and the resistances of the individual strain gauges after bonding were measured to be $R_1 = 2020$, $R_2 = 2150$, $R_3 = 2060$ and $R_4 = 2060$ ohms respectively. The strain gauge manufacturer provided the following formula for calculation of the gauge factor after allowing for strain due to mounting and slight nonlinearities in the response

$$\begin{aligned}
 GF &= \frac{157.5 + 3400(-2 \times 752.4 \times 10^{-6} + 5 \times 10^{-4})2316.5/2072.5}{172.2}
 \end{aligned} \tag{16}$$

The gauge factor specifies the relative change in gauge resistance per unit change in strain.

The reference resistances R and R_o in the bridge were measured to be 3.79 k Ω and 3.3 k Ω respectively. The bridge was balanced in the unstrained condition prior to each experiment

and analysis of the bridge circuit shows the relative change in voltage V_o/V_i due to the change in resistance of the strain gauges to be given by

$$V_o/V_i = 0.2408 \times 10^{-3} \Delta R \quad (17)$$

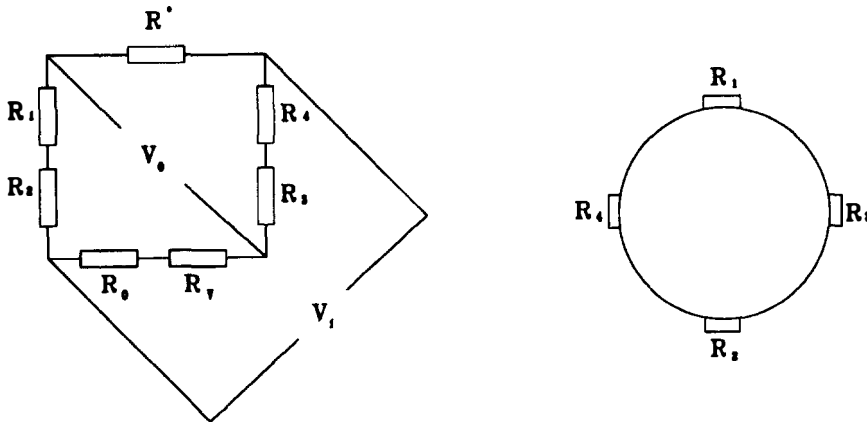


Fig.3 Arrangement of strain gauges and Wheatstone bridge. This arrangement of strain gauges on the rod and in the bridge circuit ensured the correct compensation for any bending of the rod.

Substitution of the average mounted resistance of the strain gauges gives

$$V_o/V_i = 0.4989 \Delta \bar{R} \quad (18)$$

where $\Delta \bar{R}$ is the relative change in gauge resistance.

The measured strain in the rod is therefore

$$\epsilon = \frac{V_o/V_i}{0.4989 GF} \quad (19)$$

The local force that induces the strain at the load cells is given by

$$F_L = AE\epsilon \quad (20)$$

The relationship between the local force at the load cells and the force on the upper face is obtained from the direct solution of Eq. (1) which is

$$\Delta(x,t) = \Delta(O, t - x/c_o) \quad (21)$$

so that

$$F_L(x,t) = F(O, t - x/c_o) \quad (22)$$

which is just a displacement in time. Thus the forces in Eqs. (16) and (22) are directly comparable.

EXPERIMENTAL PROCEDURE

The experimental procedure consists of releasing the sphere from the release holder which can be placed at known distances from the top surface of the rod. To calibrate the UFLC, no particle was placed on the top surface of the rod.

During single-particle impact-fracture tests, a particle of known mass and size was placed on the top face of the rod. The particle was fractured during the impact and all the fragments that resulted were collected. Usually 100 closely sized particles were fractured in each test. The voltage generated by the strain-gauge bridge during the passage of the stress wave was recorded in a storage oscilloscope (Nicolet Model 2090-III3). The signal was sampled at $2 \mu\text{s}$ intervals so that trace was completely resolved in time. A typical recorded trace without particle fracture is shown in Figure 4.

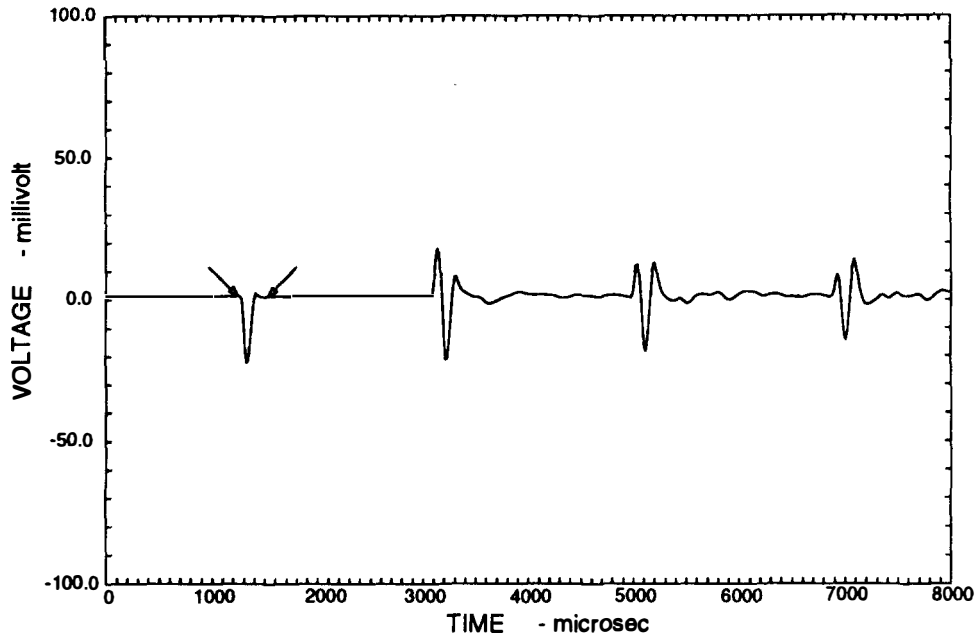


Fig.4 Typical recorded trace from the load cell bridge during a steel-on-steel calibration test.

The trace shows the passage of the primary signal followed by the original signal reflected successively from the bottom and top faces of the load-cell rod. The rod is sufficiently long to ensure that the primary signal passes the load cells completely before the first reflected signal returns. The second and subsequent reflections of the signals are significantly corrupted because the returning tensile wave does not pass the strain gauges before the compressive wave returns after reflection from the top surface.

A typical trace recorded during a single-particle impact-fracture test is shown in Figure 5. The trace reveals that the impact on the particle is much broader than for a steel-on-steel impact as shown in Figure 4. The detailed interpretation of the impact response on the particle is given later.

RESULTS

The material properties of the ball and rod are given in Table 1.

The Young's modulus of the rod was determined independently from the total time taken for the stress wave to travel from the load cells to the bottom of the rod and back. The velocity of propagation was found to be $c_0 = 5271.7 \text{ m/sec}$ and Young's modulus was calculated from Eq. (2)

$$E = \rho c_0^2 = 7788.6 \times 5271.7^2 = 21.6 \times 10^{10} \quad (23)$$

This confirms the manufacturer's value given in Table 1.

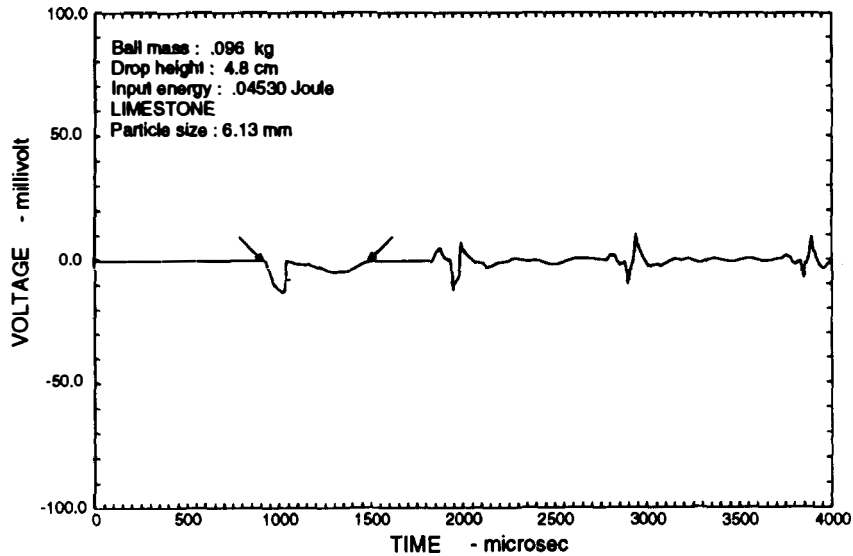


Fig.5 Typical recorded trace from the load cell bridge during an impact-fracture event.

The recorded traces were transferred to a computer for further detailed analysis. The results of four calibration experiments using four different drop heights are shown in Figures 6 to 9. The measured force, calculated from Eqs. (20) and (22), is compared with the force calculated from Eq. (16). The correspondence is remarkably good in every case confirming that the load cell is delivering an accurate representation of the force exerted on the top face of the rod. No adjustments were required to the manufacturer's gauge factor as specified in Eq. (17) so that no arbitrary constants are required to make the bridge output match the actual force in Newtons.

TABLE 1 Material properties of the ball and rod.

| | Diameter inches | Modulus of elasticity N/m ² | Poisson Ratio | Density kg/m ³ |
|------------|--------------------|--|---------------|------------------------------|
| Rod | 1 | 20.9×10^{10} | 0.3 | 7788.6 |
| Steel Ball | 3/4 | 20.3×10^{10} | 0.3 | 7833.5 |

THE ROLE OF IMPACT ENERGY IN SINGLE PARTICLE FRACTURE

The ultrafast load cell, calibrated as described above, is a very sensitive and precise device for the investigation of the impact fracture of single particles. A single particle is placed on top of the vertical rod and it can be precisely impacted by the falling sphere. The force-time history experienced by the particle during the impact is recorded. A typical result is shown in Figure 10. The deformation strain in the particle can be calculated using the momentum balance Eq. (11) for the falling sphere. The integration of the force-strain relationship allows the energy accumulated by the particle during the impact to be accurately calculated. The initiation of fracture is identified by the rapid decrease in the force exerted by the particle on the top surface of the UFLC and this is marked by the arrow in Figure 10. The residual kinetic energy of the falling sphere is absorbed by the straining and fracture of the daughter fragments that are caught between the falling sphere and the anvil. This sequence of fracture events is continued until all particles are pushed from under the sphere and a residual steel-on-steel impact occurs or until the kinetic energy

of the falling sphere is completely dissipated. In either case, the energy actually absorbed by the particle and its fracture progeny can be accurately calculated.

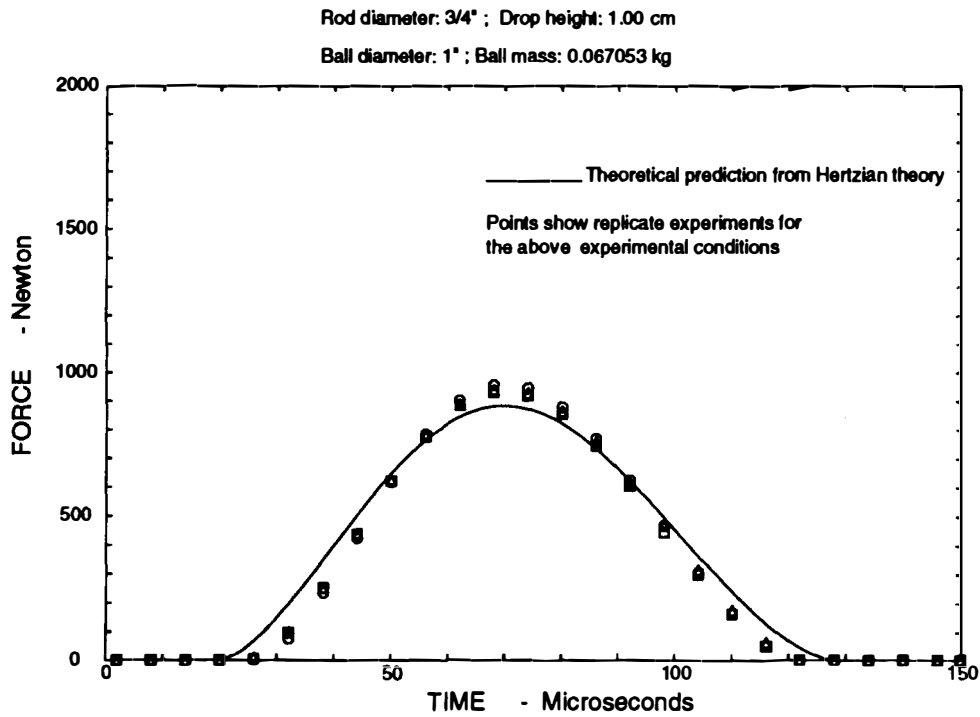


Fig.6 Comparison of the predicted and measured response from 1 cm drop height.

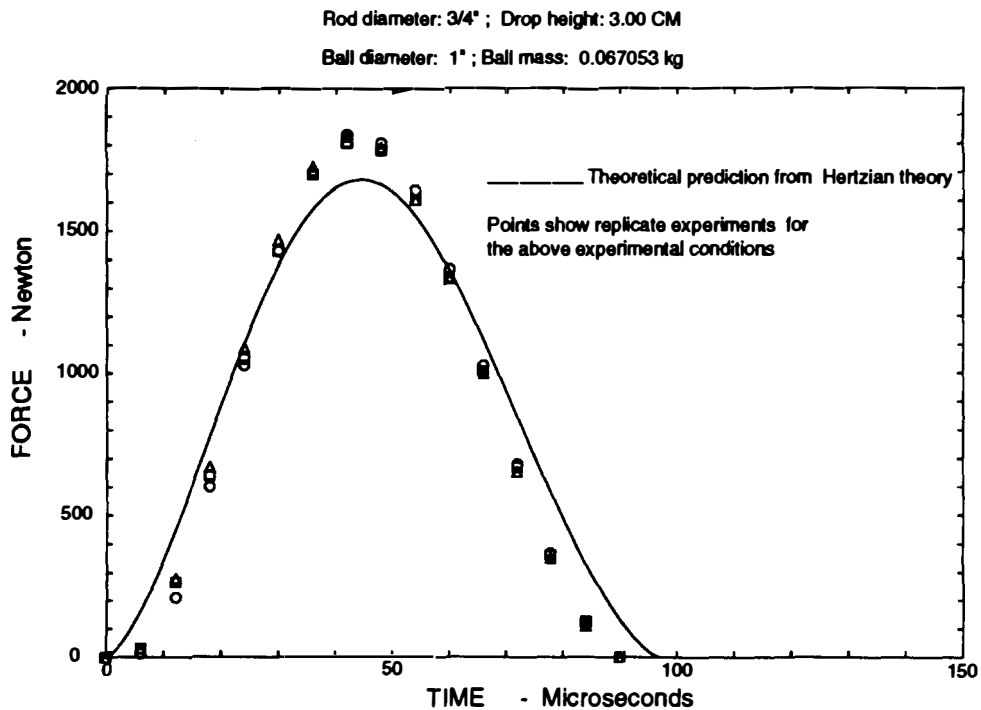


Fig.7 Comparison of the predicted and measured response from 3 cm drop height.

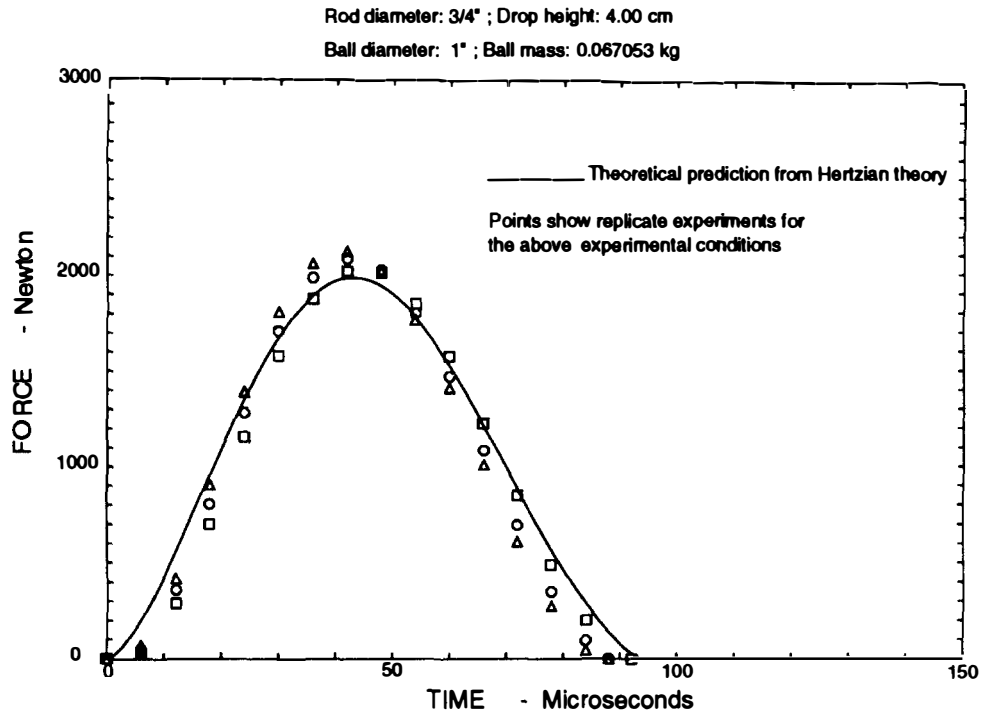


Fig.8 Comparison of the predicted and measured response from 4 cm drop height.

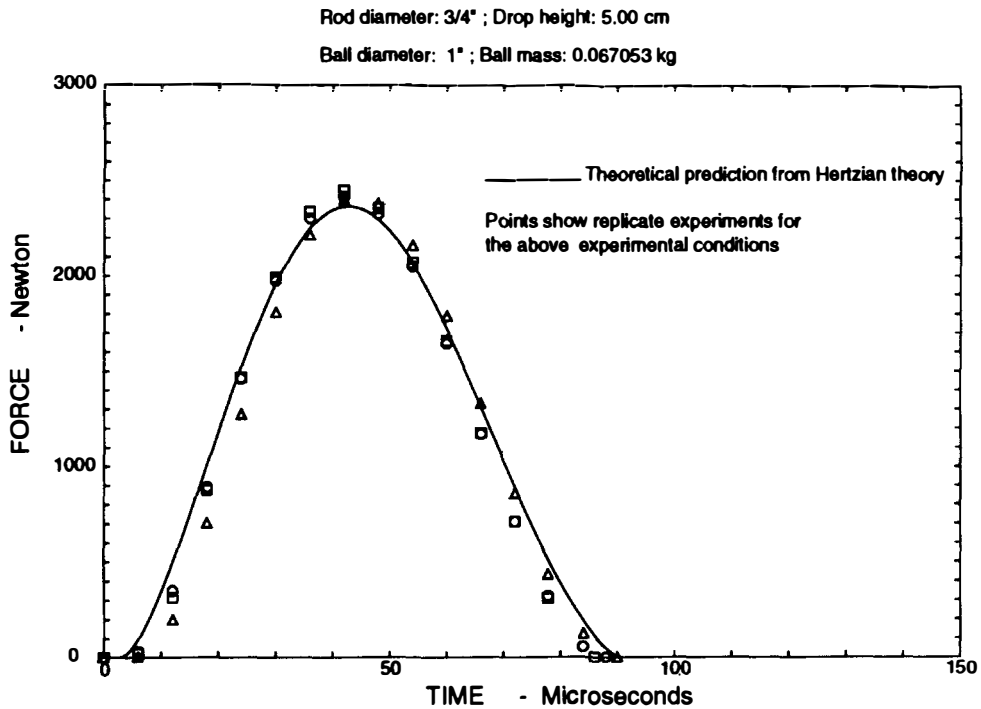


Fig.9 Comparison of the predicted and measured response from 5 cm drop height.

It is important to distinguish the effects of primary and secondary breakage when investigating the breakage function. Primary breakage refers to the first fracture that occurs when a brittle particle is subject to impact. Primary fracture can produce as few as two and as many as several tens of particles but of course no two particles will ever produce identical progeny no matter how similar they are before impact and no matter how

well the impact is controlled. Secondary breakage occurs when the daughter particles remain between the impacting surfaces and sufficient energy remains after the primary fracture to break the original progeny particles. This process is continued with the occurrence of tertiary and subsequent breakage events until all of the original impact energy is dissipated. A modified experimental technique was devised to measure the primary breakage function on the UFLC, and this will be described in a forthcoming paper. It is clear that the impact energy will have a very large effect on the breakage function that is measured during single-particle fracture experiments.

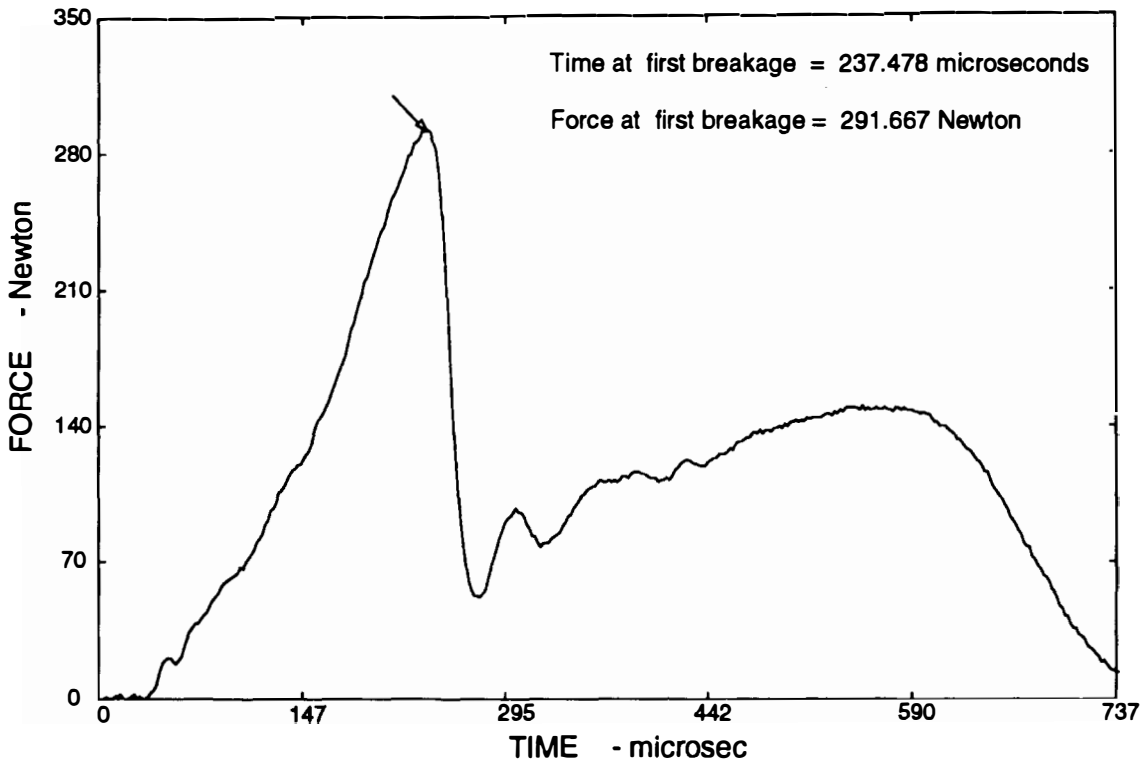


Fig.10 Typical force-time profile of a single-particle impact fracture.

The UFLC renders possible the measurement of the events which control the micromechanisms as well as the efficiency of comminution processes. The data collected on the UFLC provide a basis for the calculation of the rate of breakage and the breakage function for industrial comminution processes from the microprocesses occurring at a microscale level. The details of this new procedure are presented in Reference 7.

FRACTURE ENERGY DISTRIBUTION AND PROBABILITY OF FRACTURE OF MINERAL PARTICLES

The distribution of fracture energies in a particle population can be accurately measured by means of repetitive single particle tests. The fracture energy is the energy absorbed by the particle up to the point of first fracture. In practice it is useful to know the probability that a particle will fracture under impact loading. The correspondence between these concepts can be shown as follows. Define $F(x)$ as the probability that a particle has a fracture energy inferior or equal to x , and $G(x)$ as the probability that a particle breaks with an impact energy equal to x .

$$\begin{aligned}
 G(x) &= \text{Prob \{particle breaks under impact energy } x\} \\
 &\equiv \text{Prob \{particle fracture energy } \leq x\} \\
 &= F(x)
 \end{aligned}$$

We can then conclude that the probability that a particle breaks at a given impact energy is the same as the probability that this particle has a fracture energy inferior or equal to that same energy. This statement can be verified experimentally with the high-resolution UFLC.

For the experiment, the minerals utilized were a river bed quartz of high purity, a very fine grain limestone composed at 99% of calcite, a gold ore and a copper ore. For each particle type and size tested, one hundred particles, weighed individually, were subject to impact on the UFLC. The fracture energy of each particle was measured and normalized to the particle mass to obtain the mass specific fracture energy of the given particle. It was found that each particle type and size can be characterized by a unique distribution of mass specific fracture energies. Some examples are plotted in Figures 11, 12 and 13. All the distributions determined during this work follow a log-normal relationship. This result is in agreement with the findings of Dan and Schubert [6]. The mass specific fracture energy distribution can be expressed as follows:

$$P(E) = \frac{1}{2} \left(1 + \operatorname{erf} \left(\frac{\ln E - \mu_E}{\sqrt{2\sigma_E^2}} \right) \right) \quad (24)$$

These distributions have been measured for a variety of particle types and sizes, and the coefficients in Eq. (24) are listed in Table 2.

TABLE 2 Mass specific fracture energy distribution coefficients for a variety of ore types and sizes.

| Particle size mm * | | μ_E | σ_E^2 | E_{50} (mJ/g) |
|-----------------------|-----------|---------|--------------|--------------------|
| quartz | 3.35-4.00 | -2.5776 | 0.4407 | 76 |
| | 2.00-2.80 | -2.0333 | 0.4041 | 131 |
| | 1.40-1.70 | -1.9442 | 0.6392 | 143 |
| | 0.70-1.18 | -1.6567 | 0.4899 | 192 |
| | 0.50-0.70 | -0.9764 | 0.4977 | 380 |
| limestone | 4.00-4.75 | -2.1396 | 0.2230 | 118 |
| | 2.00-2.80 | -2.0121 | 0.2704 | 134 |
| | 1.40-1.70 | -2.0854 | 0.4234 | 125 |
| | 0.70-1.18 | -2.0809 | 0.3495 | 125 |
| | 0.50-0.70 | -1.4470 | 0.6190 | 240 |
| copper ore | 3.35-4.00 | -1.8670 | 0.3124 | 155 |
| gold ore | 3.35-4.00 | -1.5551 | 0.3197 | 210 |

* round-mesh precision 6.5" sieves

By using the medians of these fracture energy distributions, it is possible to visualize the variation of fracture energy with particle size. The values of E_{50} listed in Table 2 clearly show that specific fracture energy increases as particle size decreases in an exponential manner. This explains quantitatively why the finer the particles, the greater the energy required for comminution.

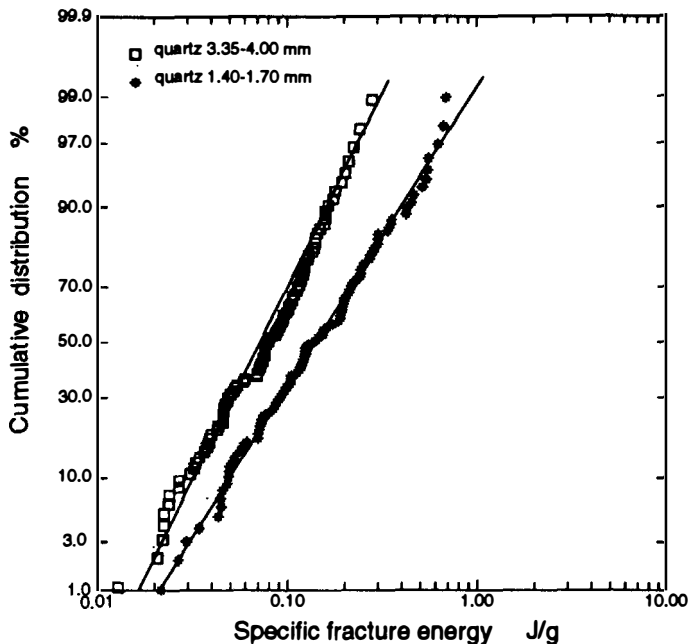


Fig.11 Mass specific fracture energy distributions for two quartz sizes.

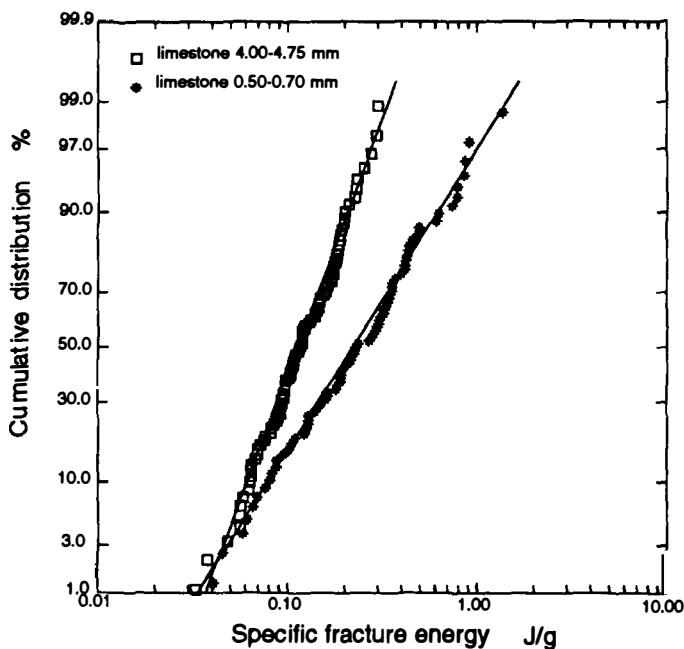


Fig.12 Mass specific energy distribution for two limestone sizes.

The probability of fracture was measured by conducting a few careful drop tests at impact energies sufficiently low so that less than 100% of the particles would break. The results obtained are displayed in Table 3 together with the values calculated from Eq. (24) using the parameters in Table 2.

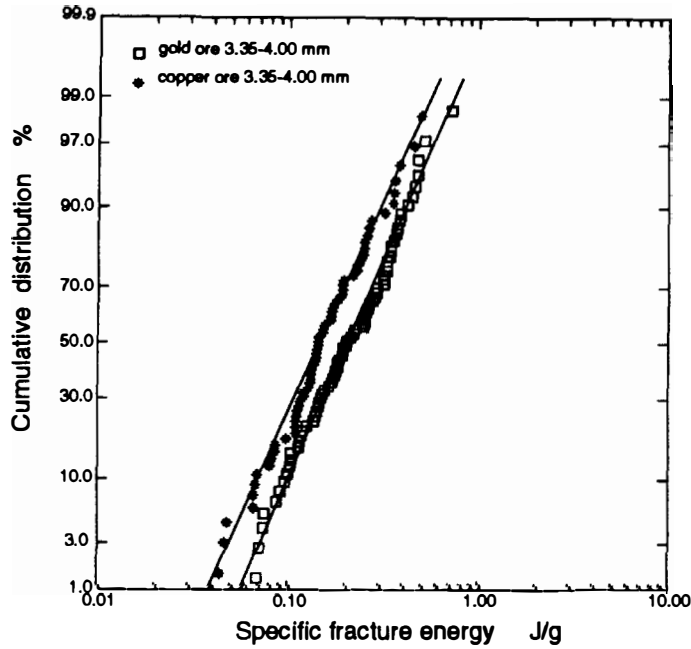


Fig.13 Mass specific fracture energy distribution for a gold ore and a copper ore.

These results confirm experimentally that the mass specific fracture energy distribution is identical to the probability of breakage for a given particle population. The distribution of mass specific fracture energy associated with a certain particle population can be generated simply by plotting its probability of breakage for various impact energies. In addition, since this study has demonstrated that the mass specific fracture energy distribution can be successfully described by a log-normal relationship, two probabilities of breakage at two different impact energies are in principle sufficient to generate the complete mass specific fracture energy distribution of a given particle population of known type and size.

TABLE 3 Experimental results on the probability of fracture of quartz and limestone particles along with their values calculated from the mass specific fracture energy distributions.

| Particle size (mm) | | Impact energy (Joule/gram) | Measured fracture probability (%) | Calculated fracture probability (%) | Error (%) |
|-----------------------|-----------|-------------------------------|--------------------------------------|--|--------------|
| quartz | 3.35-4.00 | 0.17095 | 95 | 89 | -6 |
| | | 0.09008 | 75 | 61 | -14 |
| | 2.00-2.80 | 0.35466 | 90 | 94 | +4 |
| | | 0.12255 | 42 | 46 | +4 |
| | 1.40-1.70 | 0.31000 | 84 | 83 | -1 |
| | | 0.12684 | 49 | 44 | -5 |
| limestone | 4.00-4.75 | 0.17459 | 21 | 20 | -1 |
| | 2.00-2.80 | 0.21708 | 7 | 17 | +10 |

CONCLUSIONS

The experiments have confirmed the following:

1. The measured velocity of the compressive strain wave in the measuring rod is accurate.
2. The calculated calibration of the load cells is accurate.
3. The measured strain wave is dynamically identical to the inducing force on the surface of the rod. Thus the lateral spreading of the strain wave from the small contact area on the surface across the entire cross-section of the rod is substantially completed before the wave reaches the strain gauges. Furthermore, the dissipation of strain energy during the transmission of the wave from the impact face to the gauges is negligible. The reduction of amplitude for successive reflection evident in Figure 4 is due predominantly to losses on reflection.
4. The UFLC is an accurate device for the observation of fracture events and it can be calibrated absolutely to the precision at which the material properties of the sphere and rod are known.
5. The high-resolution of the UFLC is capable of measuring very precisely the mass specific fracture energy distribution of virtually any mineral particle population. The results clearly establish that mass specific fracture energy distribution are log-normal and that the probability of fracture and fracture energy distribution are equivalent.

ACKNOWLEDGEMENTS

This research has been supported by the Department of the Interior's Mineral Institute program administered by the US Bureau of Mines through the Generic Mineral Technology Center for Comminution under grant number G1105149.

REFERENCES

1. Goldsmith, W. *Impact. The Theory and Physical Behavior of Colliding Solids*. Edward Arnold. London (1990).
2. Narayanan, S.S. Modeling the Performance of Industrial Ball Mills using Single Particle Breakage Data. *International Journal of Mineral Processing*. 20, 211 (1987).
3. Narayanan, S.S. & Whiten, W.J. Breakage Characteristics for Ores for Ball Mill Modelling. *Proc. Australas Inst. Min. Metall.* No. 286, June, (1983).
4. Narayanan, S.S. & Whiten, W.J. Determination of Comminution Characteristics from Single-Particle Breakage Tests and its Application to Ball-Mill Scale-Up. *Trans. Instn. Min. Metall.* 97, C115 (1988).
5. Pauw, O.G. & Mare, M.S. The Determination of Optimum Impact-Breakage Routes for an Ore. *Powder Technology*. 54, 3 (1988).
6. Dan, C.C. & Schubert, H. Breakage Probability, Progeny Size Distribution and Energy Utilization of Comminution by Impact, *7th European Symposium on Comminution*, Ljubljana, Yugoslavia, 1, 169 (1990).
7. King, R.P. & Bourgeois, F. A New Conceptual Model For Ball Milling, Submitted for publication, *XVIII International Mineral Processing Congress*, Sydney, Australia, (1993).